A phase field approach for the fully coupled thermo-electro-mechanical dynamics of nanoscale ferroelectric actuators

Dan Wang[1] , **Haoyuan Du**[1]**, Linxiang Wang**[1] **and Roderick Melnik**[2]

[1] State Key Laboratory of Fluid Power and Mechatronic Systems, Zhejiang University, 310027 Hangzhou, People's Republic of China
[2] MS2Dicovery Interdisciplinary Research Institute, Wilfrid Laurier University, Waterloo, ON N2L 3L5, Canada

E-mail: wanglx236@zju.edu.cn

CrossMark

Abstract

The fully coupled thermo-electro-mechanical properties of nanoscale ferroelectric actuators are investigated by a phase field model. Firstly, the thermal effect is incorporated into the commonly-used phase field model for ferroelectric materials in a thermodynamic consistent way and the governing equation for the temperature field is derived. Afterwards, the modified model is numerically implemented to study a selected prototype of the ferroelectric actuators, where strain associated with electric field-induced non-180° domain switching is employed. The temperature variation and energy flow in the actuation process are presented, which enhances our understanding of the working mechanism of the actuators. Furthermore, the influences of the input voltage frequency and the thermal boundary condition on the temperature variation are demonstrated and carefully discussed in the context of thermal management for real applications.

Keywords: thermo-electro-mechanical, phase field, ferroelectric actuator, thermal management

(Some figures may appear in colour only in the online journal)

1. Introduction

Piezoelectric materials have been used as the basic building blocks in many smart devices and structures since their discovery due to the intrinsic electromechanical coupling effects [1–6]. In particular, various types of actuators [1], sensors [2], vibration dampers [3, 4] and energy harvesters [5, 6] based on piezoelectric materials have been proposed and investigated by the research community and some of them have already been adopted for the industrial applications. However, the limited strain via the inverse piezoelectric effect is a main drawback associated with piezoelectric materials when considered for the actuation purpose [1, 7]. Efforts to improve the output strain of piezoelectric actuators have been tried by different researchers with different methods [8–14], among which new actuation mechanism employing the much larger strain associated with non-180° ferroelectric domain switching is very promising, especially for nanoscale actuation [12–14]. In nanoscale regime, the extremely large driving

electric voltage that is required at the macroscale is reduced to the level of several Volts, which can be easily powered by a voltage source on printed circuit board. In addition, the extremely complex stress state present at the macroscale, which could lead to a material failure, also disappears and the bias stress required to induce repeatable non-180° domain switching can be easily realized through a mechanical interaction with the substrate. Different prototypes of nanoscale ferroelectric actuators have been presented in the literature. For details of the actuation mechanism and process, references [13] and [14] can be referred to.

To investigate the nonlinear multiphysics coupled properties of ferroelectric materials, phase field model provides a powerful tool, which is a mesoscale model and can track the domain wall motion and domain pattern evolution in a straightforward and robust way [15–26]. With the implementation of periodic boundary conditions and semi-implicit spectrum algorithm, the constitutive relations of bulk materials have been captured [15, 16]. The influences of grain

boundary condition, grain size and input frequency on macroscopic characteristics of ferroelectric materials have been studied [17, 18]. In addition, the phase field model has also been employed by researchers to investigate the properties of ferroelectric thin films [19, 20]. Furthermore, the phase field model has already been extended to real-space simulations with finite element method, which enables us to address any nanoscale ferroelectric structures and devices with arbitrary geometries and boundary conditions [20–24]. However, most phase field models for ferroelectric materials are only electro-mechanically coupled [15–24] or only incorporate a temperature-dependent term in the phase field governing equation [25, 26]. On the other hand, domain switching is inherently a dissipative process and hysteresis is always present in the input–output relation in ferroelectric materials, which leads to a large amount of heat production. Thermal management is very important for naoscale ferroelectric devices, which calls for a fully coupled thermo-electro-mechanical phase field model. Governing equations for temperature field and considerations of thermal boundary conditions need to be included.

In the current work, a fully coupled phase field model is firstly formulated, which incorporates the effect of the temperature field in a thermodynamic consistent way [27, 28]. The modified phase field model is well-suited for the fully coupled thermo-electro-mechanical investigation of nanoscale ferroelectric devices, including nanoscale ferroelectric actuators [13, 14], ferroelectric energy harvesters [29–31] and ferroelectric memory devices [32, 33]. Useful guidance can be obtained from the fully coupled investigation, especially for the thermal management of these devices. As a demonstration, a selected prototype of the nanoscale ferroelectric actuators is systematically studied via the modified phase field model. The temperature variation and energy flow in the actuation process are presented. The influences of input frequency and thermal boundary condition on the temperature variation and actuation performance of the actuator are carefully investigated and discussed in the context of thermal management for real applications.

The paper is organized as follows. Section 2 provides the formulation of the thermo-electro-mechanically coupled phase field model. Details of the numerical implementation are described in section 3. In section 4, the simulation results of the selected prototype of the ferroelectric actuators are presented and detailed discussions are given. Section 5 highlights major conclusions drawn from the current work.

2. Model formulation

The fully coupled phase field model formulated in this section is based on the work proposed in [21]. The electro-mechanically coupled model in [21] was derived in a modern continuum mechanics way, where distinction between the fundamental balance laws and the constitutive equations is clear and the thermal effect can be easily incorporated. As in [21] and most other phase field models, small deformation is assumed in the current work. For the mechanical part, balance

of linear momentum or Newton's second law gives

$$\sigma_{ji,j} + b_i = \rho \ddot{u}_i \text{ in } V, \tag{2.1}$$

with boundary conditions:

$$\sigma_{ji} n_j = t_i \text{ on } S_t, \tag{2.2}$$

$$u_i = \hat{u}_i \text{ on } S_u, \tag{2.3}$$

where σ_{ij} denote the Cartesian components of the stress tensor, b_i the components of the external body force vector, ρ the mass density, u_i the components of the displacement vector, n_i the components of the unit normal vector of the boundary, t_i the traction applied to boundary S_t and $\hat{u}_i$ the enforced displacement on boundary S_u. Standard index notation is applied, where the repeated indices mean summation over all the values of the specific index, overdot represents a derivative with respect to time, and the subscript, j is a partial differentiation with respect to the x_j coordinate. In addition, linear kinematics assumption gives the relation between the strain components ε_{ij} and mechanical displacement as:

$$\varepsilon_{ij} = \frac{1}{2}(u_{i,j} + u_{j,i}). \tag{2.4}$$

A constitutive relation between the stress and strain tensor is further needed to make the mechanical part closed.

For the electrical part, Gauss's law yields

$$D_{i,i} - q = 0 \text{ in } V, \tag{2.5}$$

with boundary conditions:

$$D_i n_i = -\omega \text{ on } S_\omega, \tag{2.6}$$

$$\varphi = \hat{\varphi} \text{ on } S_\varphi, \tag{2.7}$$

where D_i represent the components of the electric displacement vector, q the volume charge density, ω the surface charge density, φ the electric potential and $\hat{\varphi}$ the enforced electric potential on boundary S_φ. The electric field E_i can be expressed as the negative gradient of the electric potential as:

$$E_i = -\varphi_{,i}. \tag{2.8}$$

To close the electrical part, constitutive relation between the electric displacement and electric field is needed. Considering the relation between the electric displacement, electric field and material polarization P_i:

$$D_i = P_i + \kappa_0 E_i, \tag{2.9}$$

where κ_0 is the permittivity of free space, the relation between the material polarization and electric field is exactly what is needed. As in [21], a new system of 'micro-forces' that work conjugate to the order parameter P_i is introduced and the governing equation is given as:

$$\xi_{ji,j} + \pi_i + \gamma_i = 0 \text{ in } V, \tag{2.10}$$

where ξ_{ji} are the components of the micro-force tensor, π_i the components of the internal micro-force vector and γ_i the components of the external micro-force vector. As shown in the following part, equation (2.10) leads to a generalized form of the Time-Dependent Ginzburg–Landau (TDGL) equation, where periodic boundary conditions or free traction boundary conditions are always imposed. For details of the introduced 'micro-forces' system, reference [21] can be referred to.

For the thermal part, conservation law of energy or the first law of thermodynamics gives [27, 28]:

$$\dot{e} = \sigma_{ji}\dot{\varepsilon}_{ij} + E_i\dot{D}_i + \xi_{ji}\dot{P}_{i,j} - \pi_i\dot{P}_i - q_{i,i} + g \text{ in } V, \quad (2.11)$$

with boundary conditions:

$$q_i n_i = h \text{ on } S_h, \quad (2.12)$$

$$\theta = \hat{\theta} \text{ on } S_\theta, \quad (2.13)$$

where e is the internal energy, q_i the components of the heat flux vector, g the heat source, h the normal component of the heat flux on boundary S_h, θ the temperature and $\hat{\theta}$ the enforced temperature on boundary S_θ. In solids, heat conduction is dominant. Fourier's law for heat conduction gives:

$$q_i = -k\theta_{,i}, \quad (2.14)$$

where k denotes the thermal conductivity of the material. Expression for the internal energy is further needed.

To obtain the unknown constitutive relations and expressions described above, a Helmholtz free energy is proposed, which is allowed to retain the following dependence:

$$\psi = \psi(\varepsilon_{ij}, D_i, P_i, P_{i,j}, \dot{P}_i, \theta). \quad (2.15)$$

Different from the free energy format in [21], the current one is allowed to have a dependence on the temperature. By imposing the second law of thermodynamics, the following relations can be obtained:

$$\sigma_{ji} = \frac{\partial\psi}{\partial\varepsilon_{ij}}, \ E_i = \frac{\partial\psi}{\partial D_i}, \ \xi_{ji} = \frac{\partial\psi}{\partial P_{i,j}}, \ \pi_i = -\frac{\partial\psi}{\partial P_i} - \beta\dot{P}_i,$$

$$\frac{\partial\psi}{\partial\dot{P}_i} = 0, \ s = -\frac{\partial\psi}{\partial\theta}, \ e = \psi + \theta s,$$
$$(2.16)$$

where s denotes the entropy and β represents the inverse 'mobility'. With a specific concrete expression of the Helmholtz free energy, closed form governing equations for the thermo-electro-mechanically coupled problems considered in the current work are given by the constitutive relations in equation (2.16) combined with the fundamental balance laws in equations (2.1)–(2.14). Details regarding the specification of the Helmholtz free energy are provided in appendix A. Substituting the relations in equation (2.16) into the governing equation for the 'micro-forces' system yields:

$$\left(\frac{\partial\psi}{\partial P_{i,j}}\right)_{,j} - \frac{\partial\psi}{\partial P_i} + \gamma_i = \beta\dot{P}_i, \quad (2.17)$$

which is a generalized form of the TDGL equation. Furthermore, the governing equation for the temperature field, that is equation (2.11), can be reduced as:

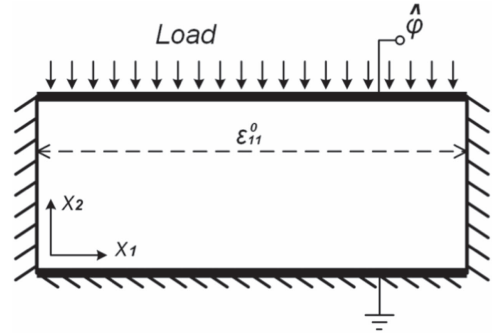$$\theta\dot{s} - \beta\dot{P}_i\dot{P}_i - k\theta_{,ii} + g = 0. \quad (2.18)$$

Figure 1. Schematic demonstration of the embedded ferroelectric actuator.

With an adiabatic thermal boundary condition and no internal heat source, the excess entropy production of the material $\theta\dot{s}$ is consisted of two parts. One is related to the viscosity effect of the domain switching, and the other to the heat conduction process.

3. Numerical implementation

In this section, the fully coupled thermo-electro-mechanical phase field model derived in section 2 is numerically implemented to study the embedded actuator proposed in [14]. A two-dimensional schematic representation of the embedded actuator is shown in figure 1. The left, right and lower three boundaries are mechanically constrained to impose an in-plane pre-strain ε_{11}^0, which favors in-plane domains with no external electric field applied. The ferroelectric material, which is assumed to be single crystal BaTiO$_3$ in the current work, is sandwiched with two compliant electrodes, through which the external electric field is applied. With a strong enough electric field, the pre-strain ε_{11}^0 favored in-plane domains will switch to the out-plane ones, and an actuation strain is obtained associated with this domain switching process. When the electric field is withdrawn, the out-plane domains will return to their initial status automatically under the influence of the pre-strain ε_{11}^0. For more details about the working mechanism of the actuator, reference [14] can be referred to.

Different from the investigation in [14], temperature variation and energy flow in the ferroelectric actuation process is carefully analyzed in the current work in the context of thermal management. Influences of different factors on the temperature variation are the research emphasis. A series of two-dimensional phase field simulations are carried out, where the coupled partial differential governing equation system, i.e. equations (2.1), (2.5), (2.17), (2.18), is numerically solved. The computational area is 90 nm × 30 nm. Important model parameters are given in appendix A. Besides, the boundary conditions for the simulations are as listed in table 1. The input voltage $\hat{\varphi}$ present in the electrical boundary condition retains the following form:

$$\hat{\varphi} = [2\sin(2\pi ft) + 2](V), \quad (3.1)$$

where f is the frequency. Consistent domain patterns obtained from numerical experiments are selected as the initial

Table 1. List of boundary conditions for the simulations.

	Left boundary	Right boundary	Lower boundary	Upper boundary
Elastic equation	$u_1 = 0$	$u_1 = \varepsilon_{11}^0 \cdot L$	$u_1 = \varepsilon_{11}^0 \cdot x$	$\sigma_{12} = 0$
	$u_2 = 0$	$u_2 = 0$	$u_2 = 0$	$\sigma_{22} = -$Load
Gauss's equation	$D_1 = 0$	$D_1 = 0$	$\phi = 0$	$\varphi = \hat{\varphi}$
Heat equation	$q_1 = 0$	$q_1 = 0$	$q_2 = 0$	$q_2 = 0 / q_2 = h_0(\theta - \theta_{\text{env}})^{\text{a}}$
TDGL equation	Free flux[b]	Free flux	Free flux	Free flux

[a] Thermal adiabatic and convective cooling conditions are respectively considered.
[b] The flux vectors for the two TDGL equations in two-dimensional case are respectively: $\Gamma_1 = \left(\frac{\partial \psi}{\partial P_{1,1}}, \frac{\partial \psi}{\partial P_{1,2}} \right)$ and $\Gamma_2 = \left(\frac{\partial \psi}{\partial P_{2,1}}, \frac{\partial \psi}{\partial P_{2,2}} \right)$. Free flux means $\boldsymbol{\Gamma} \cdot \boldsymbol{n} = 0$.

condition and the initial temperature is set as 398 K. Finite element method combined with backward time differentiation algorithm is adopted to numerically solve the governing equation system in COMSOL Multiphysics [34]. Note that domain walls in phase field model are diffusive and their width defines a characteristic length scale [21]:

$$l_0 = \sqrt{\frac{a_0 \cdot P_0}{E_0}}, \tag{3.2}$$

where P_0 is the spontaneous polarization and E_0 is the electric field value required to induce homogeneous 180° polarization switching. With the material parameters given in appendix A, the specific value for BaTiO$_3$ is 1.28 nm. Consequently, square mesh with element size equal to 1 nm is employed in the simulation, in which case, domain walls span across several elements and sufficient simulation accuracy is guaranteed.

With several numerical experiments, it is noticed that homogenized temperature can always be achieved at each solution point even with a very small thermal conductivity constant (in the order of 10^{-4} W m^{-1} K^{-1}), which means heat conduction process takes place at a rate much faster than the other phenomena. When the thermal conductivity constant is further increased to the order of 10^2 W m^{-1} K^{-1}, numerical instability occurs due to the huge difference between the characteristic time scales of the heat conduction process and other processes involved in the problem. In addition, considering the fact that the mean free path of phonons, which are the energy carriers in heat conduction process, lies in the order of 10^2 nm that are comparable to the length scale of the structure investigated in this paper, Fourier's law for heat conduction needs to be modified [35]. In the current paper, the details of the heat conduction process are simply omitted and homogenized temperature is assumed at each moment, which means equation (2.18) can be reduced to an ordinary differential equation (ODE) with respect to the temperature θ as:

$$(c_v V) \cdot \dot{\theta} + \left\{ \iint_V [(-2a_1 P_1 - 4a_2 P_1^3) \dot{P}_1 \right.$$
$$\left. + (-2a_1 P_2 - 4a_2 P_2^3) \dot{P}_2] \mathrm{d}x_1 \mathrm{d}x_2 \right\} \cdot \theta$$
$$= \iint_V \beta (\dot{P}_1^2 + \dot{P}_2^2) \mathrm{d}x_1 \mathrm{d}x_2 - \oint_S (q_1 n_1 + q_2 n_2) \mathrm{d}l, \tag{3.3}$$

where V represents the entire material volume and S denotes the boundaries of the material. The details for the derivation of the above ODE-form governing equation are presented in appendix B. Finally, equation (3.3) coupled with the partial differential equations (PDEs)—equations (2.1), (2.5), (2.17) is solved in COMSOL Multiphysics.

4. Results and discussions

4.1. Mechanism of heat production

As pointed out in the above section, in real simulations, the governing equation for the temperature is reduced as a linear ODE. However, in this case, the detailed information regarding the mechanism of heat production is blurred, especially for the one related to the domain wall motion. To illustrate the mechanism of heat production, the original PDE-form governing equation for the temperature, i.e. equation (2.18), coupled with the governing equations for the elastic field, the electrical field and the order parameters, i.e. equations (2.1), (2.5), (2.17), is numerically implemented in this subsection. An unrealistically small thermal conductivity constant, i.e. $k = 10^{-10}$ W m^{-1} K^{-1}, is assumed in the current simulation to guarantee numerical stabilities and good illustrations of the mechanism. Besides, the input voltage frequency is set as 0.1 Hz and all of the thermal boundaries are kept adiabatic. Four snapshots of the temperature field distributions along with the detailed domain patterns at four representative time points are presented in figure 2. At $t = 0.17$ T, under the influence of the external electric field, the initial pre-strain ε_{11}^0 favored in-plane domains are switching toward the out-plane ones, which is accomplished through the non-180° domain wall motion. It is noticed that high temperature is present near the domain wall, which means heat is generated near the domain wall. As the domain wall moves, polarization variation takes place near the domain wall. Due to the intrinsic polarization viscosity, heat is produced, which is proportional to the polarization variation rate according to equation (2.18). The maximum temperature difference in figure 2(a) is 0.118 K, which would be smoothed out immediately if the thermal conductivity constant k was increased to a big enough value, e.g. $k = 10^{-4}$ W m^{-1} K^{-1}, as illustrated in figure 3. In figures 2(b) and (c), homogenized temperature distributions
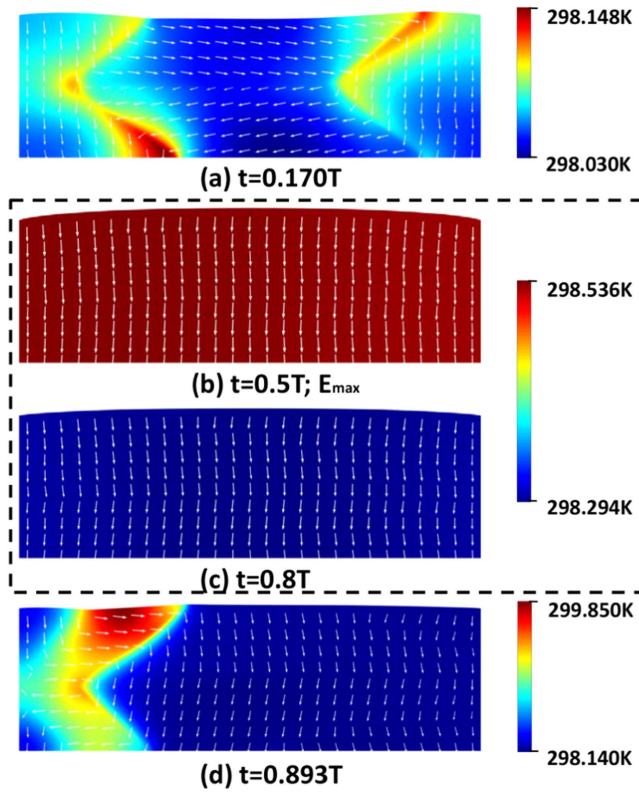
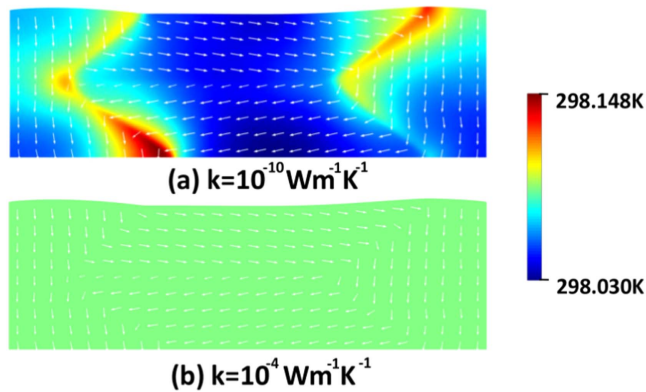**Figure 2.** Illustration of the mechanism of heat production.

Figure 3. Comparison of the temperature distribution with different thermal conductivity constant.

along with homogenized domain patterns are demonstrated, where no domain wall motion takes place. The homogenized temperature at $t = 0.8$ T is smaller than that at $t = 0.5$ T. This temperature decrease can be ascribed to the electrocaloric effect. The detailed discussion regarding electrocaloric effect is provided in the following subsection. At $t = 0.893$ T, under the influence of the substrate, the pre-strain ε_{11}^0 favored in-plane domains nucleate and expand through the domain wall motion. Similar to the results in figure 2(a), high temperature is present near the domain wall. However, it is noticed that the maximum temperature difference in figure 2(d) is 1.71 K, much larger than that shown in figure 2(a), which can be ascribed to the larger polarization variation rate. Ahead of the domain wall motion shown in figure 2(d), domain nucleation

takes place. The driving force for domain nucleation is always much larger than that for domain wall motion. With a larger driving force, the associated polarization variation takes place more rapidly; therefore, more viscosity heat is generated.

4.2. Temperature variation and energy flow in typical actuation cycles

To investigate the temperature variation and energy flow in typical actuation cycles of the ferroelectric actuator, simulations with 0.1 Hz input voltage are carried out. Adiabatic thermal boundary condition is adopted for all four boundaries. Here and in the following discussions, it is the ODE-form governing equation for the temperature coupled with PDEs for the other field variables that is solved. The domain evolution involved in a typical ferroelectric actuation cycle is demonstrated in figure 4, which is comparable to the result shown in [14]. At the initial state, most part of the actuator is covered with pre-strain ε_{11}^0 favored in-plane domains, as shown in figure 4(a). As the input voltage increases, the electric field favored out-plane domains expand through the non-180° domain wall motion, as in figures 4(b)–(d). At $t = 0.223$ T, the entire actuator is occupied by the out-plane domains. Due to the electromechanical coupling effect, an actuation strain is associated with this domain switching process. With the input voltage further increased, no domain switching takes place, but the actuation strain further increases due to the linear piezoelectric effect. At $t = 0.5$ T, a maximum actuation strain is achieved as the applied electric field reaches its peak. Afterwards, the input voltage begins to decrease. Under the influence of the substrate, out-plane domains become unstable and try to switch toward the in-plane ones. At $t = 0.892$ T, pre-strain ε_{11}^0 favored in-plane domains nucleate, as shown in figure 4(g). As the applied electric field further decreases, the in-plane domains grow at the expend of the out-plane ones. Finally, the domain patterns return to the initial state at $t = 1$ T as shown in figure 4(j), where new actuation cycles can initiate. Besides, hysteresis loops between the actuation strain and the input voltage, the charge accumulated on the upper electrode and the input voltage in this actuation cycle are presented respectively in figures 5(a) and (b). The area of the hysteresis loop in charge versus voltage relation represents the electrical work done by the external voltage source in one actuation cycle, which can be obtained from numerical integration as 11.35 nJ. In addition, the temperature variation within two typical actuation cycles is demonstrated in figure 5(c). The time axis in each cycle can be divided into four different regions. In region I and III, the temperature increases rapidly; in region II, the temperature increases first and then decreases, both in a relatively smooth way; in region IV, the temperature almost keeps constant. As discussed in the above subsection, the underlying physics for these different temperature variation modes can be attributed to two distinct basic mechanisms. One is to the viscosity associated with the domain wall motion or domain switching and the other to the electrocaloric effect [36] of the ferroelectric materials. In region I and III, electric field-induced domain switching takes place. Due to
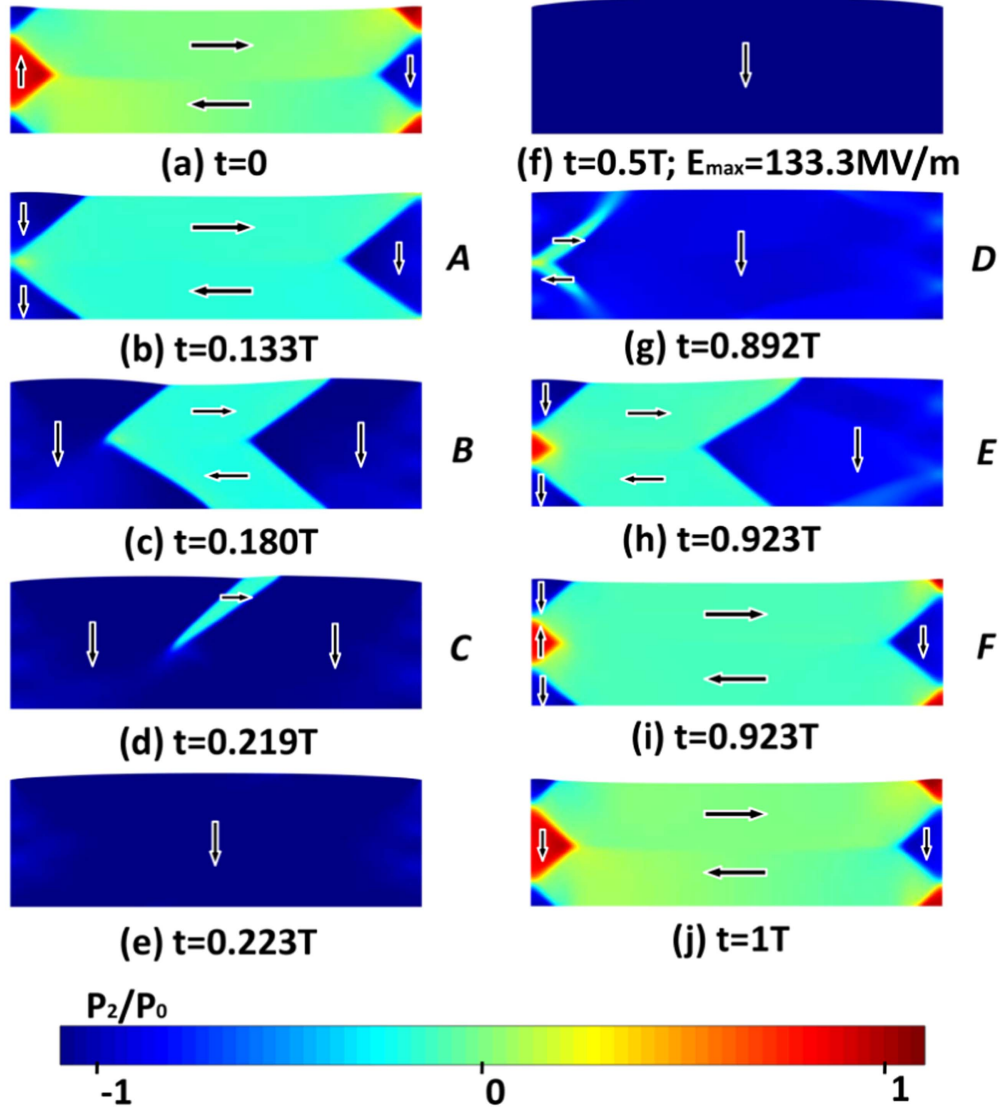
Figure 4. Demonstration of the domain switching process involved in a typical actuation cycle.

the associated viscosity effect, a large amount of heat is produced, which leads to a sharp increase of the temperature in these two regions. On the other hand, no domain switching occurs in region II and IV, where electrocaloric effect is dominant. Considering the free energy format given in appendix A, the entropy of the material can be expressed as:

$$s = -[a_1(P_1^2 + P_2^2) + a_2(P_1^4 + P_2^4)] + c_v(\ln \theta + 1), \quad (4.1)$$

which is a function of both polarization and temperature. In an isentropic process, the change of polarization can induce a temperature variation and vice verse, which is termed as electrocaloric effect and can be used for solid state refrigeration [36]. For the material considered in the current work, the temperature variation is nearly proportional to the change of the polarization magnitude under an isentropic assumption. As a reference, the polarization magnitude evolution curve is added into figure 5(c). In region II, due to the linear dielectric effect, the change of out-plane electric field strength causes a variation of the magnitude of the out-plane polarization, which further leads to a temperature variation. However, due

to the crystalline symmetry involved here, the out-plane electric field cannot alter the magnitude of the in-plane polarization, which results in a nearly constant temperature in region IV.

To demonstrate the energy flow in the actuation process, the evolution curves of the net input electrical energy and the variation of the internal energy of the actuator are presented in figure 5(d). These two curves are almost in coincidence with each other, which is a direct result of the conservation law of energy. The internal energy can be split into two different parts. One is the thermal part and the other is the temperature-independent part, which includes the Landau free energy, the mechanical energy, the electromechanical coupling energy, the domain wall energy and the electrostatic energy. To better illustrate the energy flow, the evolution curves of these two parts are also included in figure 5(d). Within a typical cycle, the net input electrical energy increases first and most of the energy is stored in the actuator in the form of temperature-independent part. After reaching the input energy peak, the stored energy begins to flow back to the external voltage
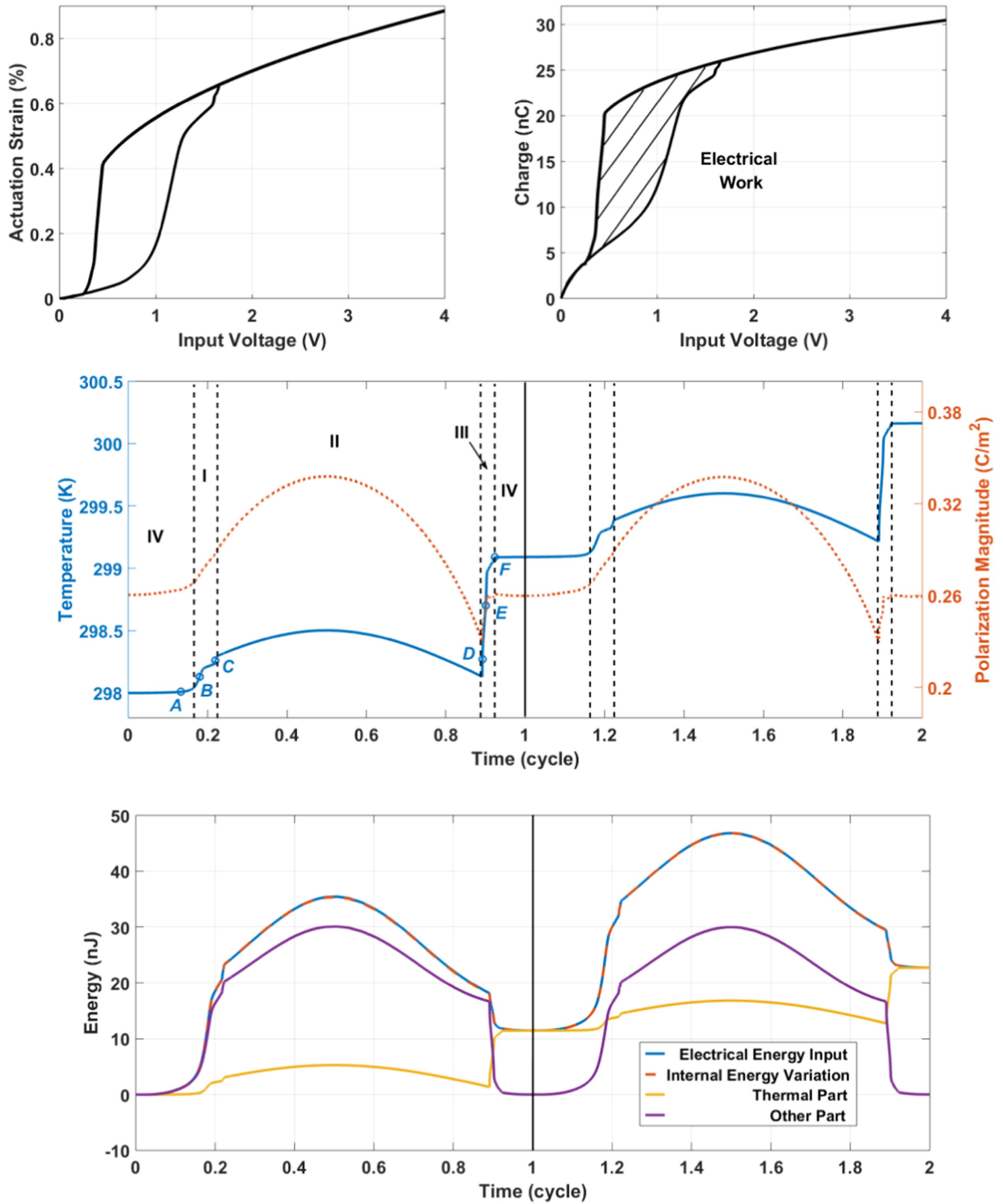
Figure 5. Demonstration of the temperature variation and energy flow in typical actuation cycles: (a) hysteresis loop between the actuation strain and the input voltage; (b) hysteresis loop between the accumulated charge and the input voltage; (c) illustration of the temperature variation in two actuation cycles; (d) illustration of the energy flow in two actuation cycles.
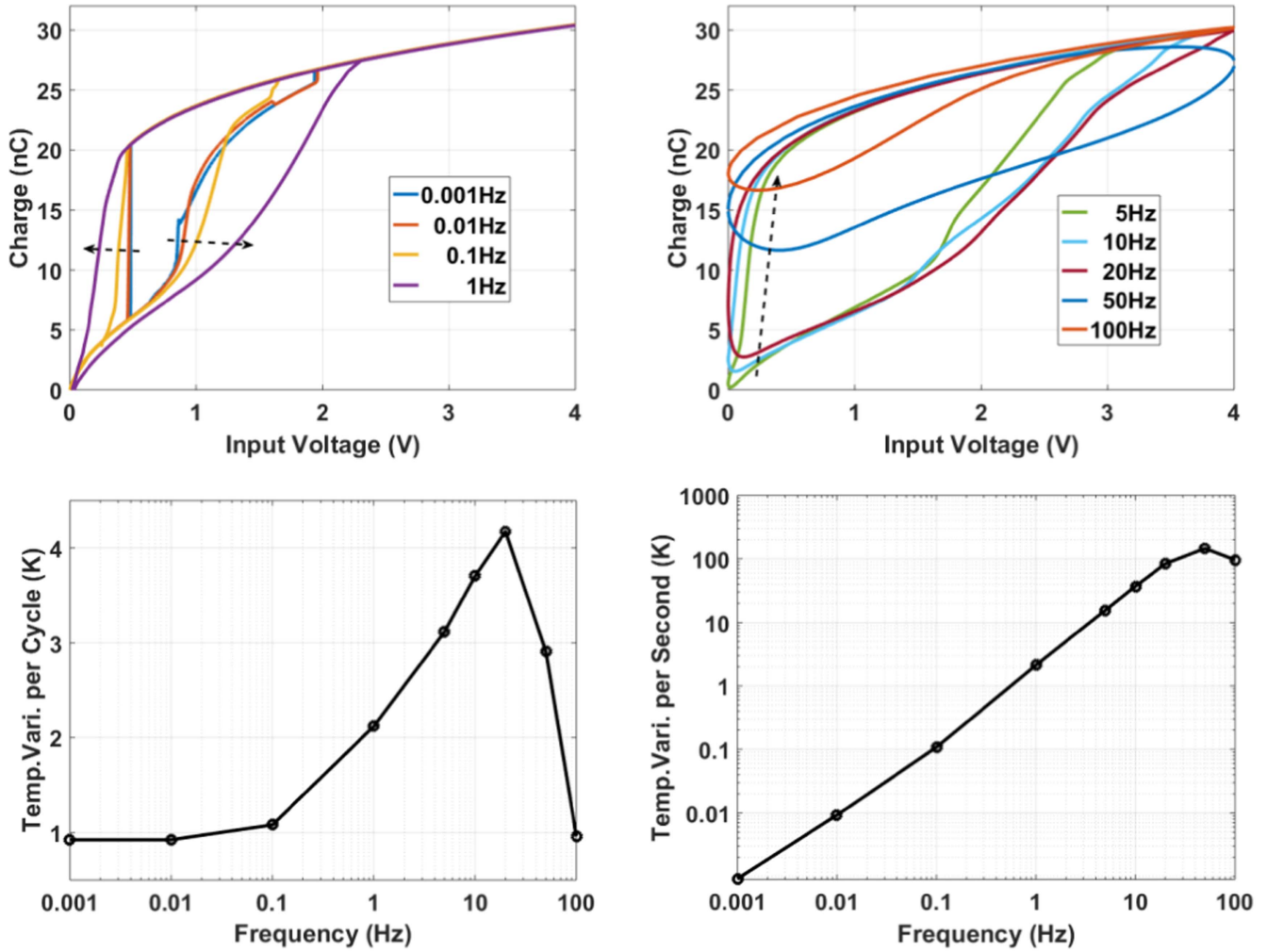
Figure 6. Demonstration of the frequency influence: (a) hysteresis loops between the charge and the input voltage in low frequency range; (b) hysteresis loops in high frequency range; (c) frequency influence on temperature variation per cycle; (d) frequency influence on temperature variation per second.

source and the total amount of the net input electrical energy decreases. However, after a complete cycle, a net work is still done by the external source due to the existence of the hysteresis phenomenon, and the work is converted to heat or the thermal part of the internal energy $C_v \Delta \theta V$, which can be numerically obtained as 11.3 nJ comparable to the value of the net work obtained above.

4.3. Frequency influence

Domain switching in ferroelectric materials is inherently a rate-dependent process [17], which means the frequency of the input voltage will have an impact on the performance of the nanoscale ferroelectric actuators. Simulations with different input frequencies are carried out. As in the above simulation, adiabatic boundary condition is assumed. The hysteresis loops between the charge and input voltage are demonstrated in figures 6(a) and (b). In the low frequency range (0.001–1 Hz), the hysteresis loop gets fatter with a higher input frequency. Larger area of the hysteresis loop means larger heat production in one actuation cycle. In the high frequency range (5–100 Hz), as the frequency increases,

more and more parts of the domain cannot follow the change of the input voltage which is proven by the flatter hysteresis loops as sketched in figure 6(b). Thus, in the entire frequency range (0.001–100 Hz) considered in the current work, as the input frequency increases, the temperature variation per cycle increases first and then decreases, as shown in figure 6(c). The maximum temperature variation is about 4 K/cycle at 20 Hz. Besides, the evolution curve of the temperature variation per unit time or per second, which incorporates the influence of the time period of the actuation cycle, is presented in figure 6(d). A maximum temperature variation 150 K s^{-1} is obtained at 50 Hz, which means the actuator fails within several seconds in this condition (adiabatic thermal boundary is imposed).

4.4. Thermal boundary condition influence

In the above simulations, adiabatic thermal boundary condition is assumed to focus on investigating the mechanism of heat production. Depending on the working condition of real applications, radiative or convective boundary condition is more reasonable. For instance, when the nanoscale devices
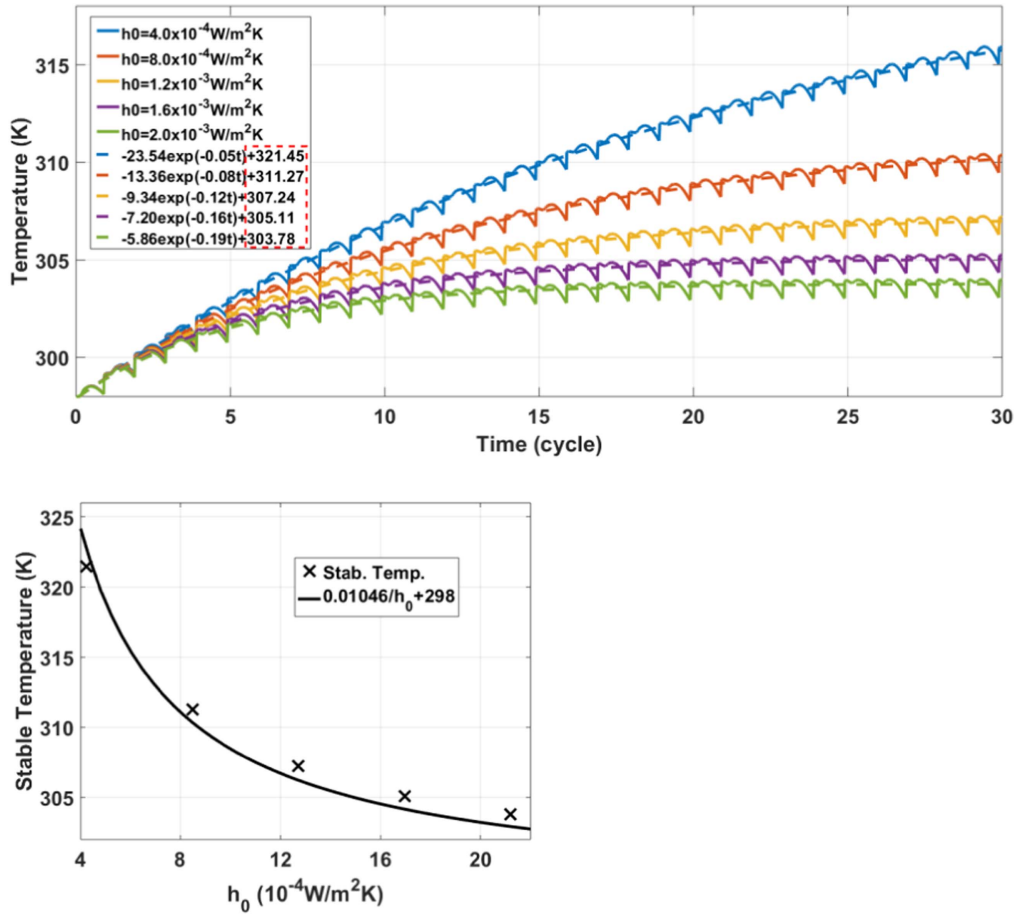
Figure 7. Demonstration of the thermal boundary condition influence: (a) temperature evolution in thirty cycles for five different convective coefficients; (b) relationship between the mean stable temperature and the convective coefficient.

are vacuum packaged and in a high temperature status, radiative heat transfer is dominant and radiative boundary conditions are preferred. Convective conditions can be applied when the devices work in flowing fluid, which is the case when the above actuator works as a nanoscale pump. To investigate the influence of the thermal boundary condition, convective conditions with different convective coefficients are adopted in this subsection (for the upper boundary only). The governing equation for the boundary condition can be expressed as:

$$h = h_0(\theta - \theta_{\mathrm{env}}), \quad (4.2)$$

where h_0 denotes the convective coefficient, which can be influenced by the material property of the fluid, the surface status of the actuator and the velocity of the fluid; θ_{env} represents the temperature of the environment, that is the fluid temperature, and is set as 298 K in the current paper. Temperature variation curves with five different h_0 values are presented in figure 7(a). All the simulations last for 30 cycles with an initial temperature 298 K. The frequency of the input voltage is selected as 0.1 Hz. As the temperature increases, the temperature difference between the actuator and surrounding fluid increases, which leads to a larger heat flux at the boundary. When the heat produced inside the actuator is balanced with the heat lost at the boundary in each cycle, stable cyclic temperature can be reached. Within 30 cycles,

the stable cyclic temperature is nearly reached for $h_0 \geqslant 1.2 \times 10^{-3}\,\mathrm{W\,m^{-2}\,K^{-1}}$. However, for the case $h_0 < 1.2 \times 10^{-3}\,\mathrm{W\,m^{-2}\,K^{-1}}$, the mean value of the cyclic temperature is still increasing. Due to the limit of the computational resources, further simulations are not carried out. Instead, the temperature curve is fitted with an exponential function with the following form:

$$\theta = a \cdot \mathrm{e}^{(b \cdot t)} + c, \quad (4.3)$$

where a, b and c are the coefficients to be fitted and it is reasonable to regard the fitted value of c as the mean stable temperature. The corresponding values are listed in figure 7(a). Furthermore, from the energy balance, a simple relation between the mean stable temperature and the convective coefficient can be obtained. Heat production per second due to domain switching can be approximated by $C_v \Delta\theta_s V$, where $\Delta\theta_s$ is the temperature variation per second. The variation of $\Delta\theta_s$ with respect to the input frequency is shown in figure 6(d). Heat loss at the boundary due to heat convection is $h_0(\theta_{\mathrm{sta}} - \theta_{\mathrm{env}})S_h$. Energy balance gives:

$$C_v \Delta\theta_s V = h_0(\theta_{\mathrm{sta}} - \theta_{\mathrm{env}})S_h, \quad (4.4)$$

which leads to:

$$\theta_{\mathrm{sta}} = \frac{C_v \Delta\theta_s V}{S_h h_0} + \theta_{\mathrm{env}}. \quad (4.5)$$

A larger convective coefficient leads to a smaller mean stable temperature. Therefore, the mean stable temperature obtained from curve fitting in figure 7(a) is further fitted with a function with the following form:

$$\theta_{\text{sta}} = \frac{m}{h_0} + 398, \qquad (4.6)$$

which retains a similar format as equation (4.5). The excellent fitting results are presented in figure 6(b), which gives a confirmation of the above analysis.

Useful guidance can be obtained from figures 7(b) and 6(d) for the thermal management of the ferroelectric actuators. The minimum allowable convective coefficient is determined by the maximum allowable working temperature. In particular, for actuators that work at 0.1 Hz, the specific value of the allowable convective coefficient can be obtained directly from figure 7(b). On the other hand, from equation (4.5), the mean stable temperature is determined by the ratio of $\Delta\theta_s$ and h_0. For actuators working at a distinct frequency, $\Delta\theta_s$ is different. To obtain a same mean stable temperature, h_0 needs to be changed accordingly to keep the ratio constant, and the information about $\Delta\theta_s$ at different frequencies is provided in figure 6(d).

5. Conclusion

A fully coupled thermo-electro-mechanical phase field model for ferroelectric materials has been formulated. The effect of temperature field has been included in a thermodynamic consistent way. The modified phase field model has been numerically implemented to systematically investigate an embedded ferroelectric actuator, which is based on electric field-induced non-180° ferroelectric domain switching. Temperature variation and energy flow in typical actuation cycles have been demonstrated, which enhances the understanding of the working mechanism of the actuator. Besides, the influences of input frequency and thermal boundary condition have also been investigated and discussed. Temperature variation rate up to 150 K s^{-1} has been obtained from simulations with 50 Hz input frequency and adiabatic thermal boundary condition. Method to determine the allowable convective coefficient has been provided for the purpose of thermal management of the ferroelectric actuator. Furthermore, the model and method formulated in the current paper is also well-suited for fully coupled thermo-electro-mechanical investigation of other nanoscale ferroelectric devices.

Appendix A. Helmholtz free energy and model parameters

The Helmholtz free energy adopted in the current work retains the following form:

$$
\begin{aligned}
\psi(\varepsilon_{ij}, D_i, P_i, P_{i,j}, \theta) =\ & a_1(\theta - \theta_1)(P_1^2 + P_2^2) \\
& + (a_2(\theta - \theta_2) + \delta)(P_1^4 + P_2^4) + a_3 P_1^2 P_2^2 \\
& + a_4(P_1^6 + P_2^6) + a_5(P_1^4 P_2^2 + P_1^2 P_2^4) + a_6 P_1^4 P_2^4 \\
& - b_1(\varepsilon_{11} P_1^2 + \varepsilon_{22} P_2^2) - b_2(\varepsilon_{11} P_2^2 + \varepsilon_{22} P_1^2) \\
& - b_3(\varepsilon_{12} + \varepsilon_{21}) P_1 P_2 \\
& + c_1(\varepsilon_{11}^2 + \varepsilon_{22}^2) + c_2 \varepsilon_{11} \varepsilon_{22} + c_3(\varepsilon_{12}^2 + \varepsilon_{21}^2) \\
& + a_0(P_{1,1}^2 + P_{1,2}^2 + P_{2,1}^2 + P_{2,2}^2) \\
& + \frac{1}{2\kappa_0}((D_1 - P_1)^2 + (D_2 - P_2)^2) - c_v \theta \ln\theta, \qquad (A.1)
\end{aligned}
$$

where $a_0 \sim a_6$, $b_1 \sim b_3$, $c_1 \sim c_3$, θ_1, θ_2, δ and c_v are material-specific parameters, which can be obtained by fitting with the properties of the considered materials. The specific values of these parameters used in the simulations (for BaTiO$_3$) are as follows:

$a_1 = 3.3 \times 10^5$ Nm^2 C^{-2} K^{-1}, $a_2 = 3.6 \times 10^6$ Nm^6 C^{-4} K^{-1},
$a_3 = 1.5 \times 10^7$ Nm^6 C^{-4}, $a_4 = 6.6 \times 10^9$ Nm^{10} C^{-6},
$a_5 = 2.9 \times 10^9$ Nm^{10} C^{-6}, $a_6 = 1 \times 10^{13}$ Nm^{14} C^{-8},
$b_1 = 1.3 \times 10^{10}$ Nm^2 C^2, $b_2 = -9.7 \times 10^8$ Nm^2 C^2,
$b_3 = 6.4 \times 10^9$ Nm^2 C^2, $c_1 = 6.7 \times 10^{10}$ Nm^{-2},
$c_2 = 4.4 \times 10^{10}$ Nm^{-2}, $c_3 = 1.1 \times 10^{11}$ Nm^{-2},
$a_0 = 2 \times 10^{-10}$ Nm^4 C^{-2}, $c_v = 3.9 \times 10^6$ Nm^{-2} K^{-1},
$\theta_1 = 383$ K, $\theta_2 = 448$ K, $\delta = 7.3 \times 10^8$ Nm^6 C^{-4}.

Parameters $a_1 \sim a_5$, $b_1 \sim b_3$, $c_1 \sim c_3$, θ_1, θ_2 and δ are taken from [37], where some necessary transformations and calculations are needed. a_6 is from [38]; a_0 from [21] and c_v from [25]. The term $a_6 P_1^4 P_2^4$ in equation (A.1) was firstly added into the free energy in [38] to allow for simultaneous adjustments of the dielectric properties and the energy barriers for non-180° switching. Besides, other parameters needed for the simulations take the following values:

$$\kappa_0 = 8.854 \times 10^{-12} \text{ N}^{-1} \text{ m}^{-2} \text{ C}^2, \quad \beta = 2.5 \times 10^5 \text{ Nm}^2 \text{ C}^{-2} \text{ s},$$

where β is taken from [17].

Appendix B. Derivation of the ODE-form governing equation for the temperature

With the Helmholtz free energy given in appendix A, the specific form of the entropy of the material can be expressed as:

$$s = -[a_1(P_1^2 + P_2^2) + a_2(P_1^4 + P_2^4)] + c_v(\ln\theta + 1). \quad (B.1)$$

Therefore, the time derivative of the entropy is given as:

$$\dot{s} = (-2a_1 P_1 - 4a_2 P_1^3)\dot{P}_1 + (-2a_1 P_2 - 4a_2 P_2^3)\dot{P}_2 + c_v \frac{1}{\theta}\dot{\theta}. \quad \text{(B.2)}$$

Plugging equation (B.2) into equation (2.18) leads to the specific form of the governing equation for the temperature:

$$c_v \dot{\theta} + [(-2a_1 P_1 - 4a_2 P_1^3)\dot{P}_1 + (-2a_1 P_2 - 4a_2 P_2^3)\dot{P}_2]$$
$$\times \theta - \beta(\dot{P}_1^2 + \dot{P}_2^2) - k(\theta_{,11} + \theta_{,22}) + g = 0, \quad \text{(B.3)}$$

which is a PDE with respect to the temperature. Considering the fact that homogenized temperature is assumed and no internal thermal sources or sinks exist, the last two terms in equation (B.3) can be omitted and the equation can be reduced as:

$$c_v \dot{\theta} + [(-2a_1 P_1 - 4a_2 P_1^3)\dot{P}_1 + (-2a_1 P_2 - 4a_2 P_2^3)\dot{P}_2]$$
$$\times \theta - \beta(\dot{P}_1^2 + \dot{P}_2^2) = 0. \quad \text{(B.4)}$$

Integrating equation (B.4) within the entire material domain gives:

$$(c_v V) \cdot \dot{\theta} + \left\{ \iint_V [(-2a_1 P_1 - 4a_2 P_1^3)\dot{P}_1 \right.$$
$$+ (-2a_1 P_2 - 4a_2 P_2^3)\dot{P}_2] \mathrm{d}x_1 \mathrm{d}x_2 \left. \right\} \cdot \theta$$
$$- \iint_V \beta(\dot{P}_1^2 + \dot{P}_2^2) \mathrm{d}x_1 \mathrm{d}x_2 = 0. \quad \text{(B.5)}$$

Further considering the effect of the heat flux on the boundaries of the material, the above governing equation for temperature can be reformed as:

$$(c_v \cdot V)\dot{\theta} + \left\{ \iint_V [(-2a_1 P_1 - 4a_2 P_1^3)\dot{P}_1] \right.$$
$$+ (-2a_1 P_2 - 4a_2 P_2^3)\dot{P}_2] \mathrm{d}x_1 \mathrm{d}x_2 \left. \right\} \theta$$
$$= \iint_V \beta(\dot{P}_1^2 + \dot{P}_2^2) \mathrm{d}x_1 \mathrm{d}x_2 - \oint_S (q_1 n_1 + q_2 n_2) \mathrm{d}l, \quad \text{(B.6)}$$

which is a linear ODE with respect to the temperature.

ORCID iDs

Dan Wang ● https://orcid.org/0000-0003-0563-8030

References

[1] Niezrecki C, Brei D, Balakrishnan S and Moskalik A 2001 Piezoelectric actuation: state of the art *Shock Vib. Dig.* **33** 269–80

[2] Shen Z, Tan C Y, Yao K, Zhang L and Chen Y F 2016 A miniaturized wireless accelerometer with micromachined piezoelectric sensing element *Sensors Actuators* A **241** 113–9

[3] Badel A, Sebald G, Guyomar D, Lallart M, Lefeuvre E, Richard C and Qiu J 2006 Piezoelectric vibration control by synchronized switching on adaptive voltage sources: towards wideband semi-active damping *J. Acoust. Soc. Am.* **119** 2815–25

[4] Lossouarn B, Deü J F, Aucejo M and Cunefare K A 2016 Multimodal vibration damping of a plate by piezoelectric coupling to its analogous electrical network *Smart Mater. Struct.* **25** 115042

[5] Priya S and Inman D J 2009 *Energy Harvesting Technologies.* (New York: Springer)

[6] Yang Z, Zu J, Luo J and Peng Y 2017 Modeling and parametric study of a force-amplified compressive-mode piezoelectric energy harvester *J. Intell. Mater. Syst. Struct.* **28** 357–66

[7] Conway N J, Traina Z J and Kim S G 2007 A strain amplifying piezoelectric MEMS actuator *J. Micromech. Microeng.* **17** 781

[8] Park S E and Shrout T R 1997 Ultrahigh strain and piezoelectric behavior in relaxor based ferroelectric single crystals *J. Appl. Phys.* **82** 1804–11

[9] Webber K G, Zuo R and Lynch C S 2008 Ceramic and single-crystal (1–*x*) PMN–*x*PT constitutive behavior under combined stress and electric field loading *Acta Mater.* **56** 1219–27

[10] Fu J, Zuo R, Qi H, Zhang C, Li J and Li L 2014 Low electric-field driven ultrahigh electrostrains in Sb-substituted (Na, K) NbO$_3$ lead-free ferroelectric ceramics *Appl. Phys. Lett.* **105** 242903

[11] Li F, Wang Q and Miao H 2017 Giant actuation strain nearly 0.6% in a periodically orthogonal poled lead titanate zirconate ceramic via reversible domain switching *J. Appl. Phys.* **122** 074103

[12] Burcsu E, Ravichandran G and Bhattacharya K 2000 Large strain electrostrictive actuation in barium titanate *Appl. Phys. Lett.* **77** 1698–700

[13] Bhattacharya K and James R D 2005 The material is the machine *Science* **307** 53–4

[14] Balakrishna A R, Huber J E and Landis C M 2014 Nano-actuator concepts based on ferroelectric switching *Smart Mater. Struct.* **23** 085016

[15] Wang J, Shi S Q, Chen L Q, Li Y and Zhang T Y 2004 Phase-field simulations of ferroelectric/ferroelastic polarization switching *Acta Mater.* **52** 749–64

[16] Soh A K, Song Y C and Ni Y 2006 Phase field simulations of hysteresis and butterfly loops in ferroelectrics subjected to electro-mechanical coupled loading *J. Am. Ceram. Soc.* **89** 652–61

[17] Su Y, Liu N and Weng G J 2015 A phase field study of frequency dependence and grain-size effects in nanocrystalline ferroelectric polycrystals *Acta Mater.* **87** 293–308

[18] Li X and Wang J 2016 Effect of grain size on the domain structures and electromechanical responses of ferroelectric polycrystal *Smart Mater. Struct.* **26** 015013

[19] Li Y L, Hu S Y, Liu Z K and Chen L Q 2001 Phase-field model of domain structures in ferroelectric thin films *Appl. Phys. Lett.* **78** 3878–80

[20] Chen L Q 2008 Phase-field method of phase transitions/ domain structures in ferroelectric thin films: a review *J. Am. Ceram. Soc.* **91** 1835–44

[21] Su Y and Landis C M 2007 Continuum thermodynamics of ferroelectric domain evolution: theory, finite element implementation, and application to domain wall pinning *J. Mech. Phys. Solids* **55** 280–305

[22] Dayal K and Bhattacharya K 2007 A real-space non-local phase-field model of ferroelectric domain patterns in complex geometries *Acta Mater.* **55** 1907–17

[23] Schrade D, Mueller R, Xu B X and Gross D 2007 Domain evolution in ferroelectric materials: a continuum phase field model and finite element implementation *Comput. Methods Appl. Mech. Eng.* **196** 4365–74

[24] Wang J and Kamlah M 2009 Three-dimensional finite element modeling of polarization switching in a ferroelectric single domain with an impermeable notch *Smart Mater. Struct.* **18** 104008

[25] Wang J, Liu M, Zhang Y, Shimada T, Shi S Q and Kitamura T 2014 Large electrocaloric effect induced by the multi-domain to mono-domain transition in ferroelectrics *J. Appl. Phys.* **115** 164102

[26] Woldman A Y and Landis C M 2016 Phase-field modeling of ferroelectric to paraelectric phase boundary structures in single-crystal barium titanate *Smart Mater. Struct.* **25** 035033

[27] Petrou Z 2013 Thermo-electro-mechanical behavior of ferroelectric nanodots *Master Thesis* The University of Texas, Austin

[28] Woldman A Y 2018 Phase-field modeling of the thermo-electro-mechanically coupled behavior of ferroelectric materials *Doctoral Dissertation* The University of Texas, Austin

[29] Münch I, Krauß M, Landis C M and Huber J E 2011 Domain engineered ferroelectric energy harvesters on a substrate *J. Appl. Phys.* **109** 104106

[30] Münch I, Krauß M, Wagner W and Kamlah M 2012 Ferroelectric nanogenerators coupled to an electric circuit for energy harvesting *Smart Mater. Struct.* **21** 115026

[31] Balakrishna A R and Huber J E 2016 Nanoscale domain patterns and a concept for an energy harvester *Smart Mater. Struct.* **25** 104001

[32] Rana D S, Kawayama I, Mavani K, Takahashi K, Murakami H and Tonouchi M 2009 Understanding the nature of ultrafast polarization dynamics of ferroelectric memory in the multiferroic $BiFeO_3$ *Adv. Mater.* **21** 2881–5

[33] Van Lich L, Shimada T, Sepideh S, Wang J and Kitamura T 2017 Multilevel hysteresis loop engineered with ferroelectric nano-metamaterials *Acta Mater.* **125** 202–9

[34] Comsol multiphysics finite element analysis software www.comsol.com

[35] Chen G 2005 *Nanoscale Energy Transport and Conversion: A Parallel Treatment of Electrons, Molecules, Phonons, and Photons* (Oxford: Oxford University Press)

[36] Scott J F 2011 Electrocaloric materials *Annu. Rev. Mater. Res.* **41** 229–40

[37] Pertsev N A, Zembilgotov A G and Tagantsev A K 1998 Effect of mechanical boundary conditions on phase diagrams of epitaxial ferroelectric thin films *Phys. Rev. Lett.* **80** 1988

[38] Zhang W and Bhattacharya K 2005 A computational model of ferroelectric domains: I. Model formulation and domain switching *Acta Mater.* **53** 185–98